サクションを考慮した粒子法の開発と斜面崩壊解析への適用

中　道　洋　平　　杉　江　茂　彦

Development of Meshless Method Considering Effect of Suction and its Application to Numerical Analysis of Slope Failure

Yohei Nakamichi　Shigehiko Sugie

Abstract

In Japan, where 70% of the area is mountainous, landslides due to rainfall occur frequently. To develop efficient countermeasures and disaster prevention plans, a numerical analysis that can consistently evaluate slope stability and slope failure is desired. This paper presents numerical analyses of slope failures induced by rainfall using the meshless method, which is suitable for large deformation problems. To analyze the effects of rainwater infiltration, two series of parametric studies are performed. The results indicate that the scale of slope failure, shape of collapse, and time to slope failure are governed by degree of saturation, water retention, and permeability.

概　　要

国土の約7割が山地である日本では豪雨に伴う斜面崩壊が起こりやすく、鉄道や高速道路をはじめとするインフラや住宅地付近では崩壊の防止や予測が重要な課題となっている。特に近年、想定を上回る激しい豪雨が観測されており、ハードとソフトの両面からの対策が求められている。降雨時の斜面は雨水の浸透に応じて時々刻々と状態が変化することから、安定した状態から崩壊に至るまでを一貫して予測できる解析技術が望まれる。本研究では、地盤の大変形問題に適した粒子法を用いて、降雨による斜面崩壊解析を実施した。解析では、地盤への雨水の浸透特性に着目したパラメトリックスタディーを実施した。その結果、地盤の飽和度および保水性の違いにより、斜面の崩壊規模や崩壊形状、崩壊に至るまでの時間が異なることが分かった。

1. Introduction

Slope failures induced by rainfall occur frequently in Japan, where approximately 70% of the land area is mountains. These adversely affect various types of infrastructure, such as expressways and railways. Once a slope failure occurs, extensive time to rebuild and substantial costs for the process of recovery are often required. Human lives are also at risk when a slope failure occurs near a residential area. Therefore, slope failures are considered one of the most significant obstacles in geotechnical engineering, and many studies have focused on them.

Recently, extreme rainfall patterns occurring locally have been observed frequently in addition to long-term conventional patterns that have a wider distribution because of climate change caused by global warming. Consequently, landslide disasters, including slope failures, have also been increasing. In 2018, there were 3,459 disasters, which was the highest number ever recorded since data collection began in 1982[1)]. In 2019, the number of landslide disasters was 1,996, which ranks fourth among the highest number of disasters on record[1)].

Most of the studies on slope failures have focused on the evaluation of slope stability and the performance of countermeasures. This is because structural countermeasures have been adopted to prevent or suppress slope failures. However, it is unrealistic to take structural countermeasures on every slope that is at risk of failure on account of an increase in landslide disasters[1)]. Hence, in recent years, there has been a surge in research focusing on non-structural measures, such as predictions and monitoring. Numerical analyses that can consistently evaluate slope stability to a scale of slope failure are strongly desired, as these are necessary for developing countermeasures and disaster prevention plans efficiently.

This paper presents the numerical analyses of slope failures induced by rainfall using the meshless method, which is suitable for large deformation problems in geotechnical engineering. First, the new meshless method formulation considering the effects of suction, which is essential to treat unsaturated soil, was proposed. Second, the proposed method was verified through a numerical analysis of the experiment on unsaturated soil. Finally, numerical analyses of the slope failures induced by rainfall were conducted. Focusing on rainwater infiltration characteristics of unsaturated soils, the effects of soil saturation, water retention, and permeability on a scale of slope failure, as well as the time until a slope failure occurs, were examined.

In this paper, it is assumed that the stresses and strains are positive for tension, whereas pore water pressure is positive for compression.

2. Numerical method

2.1 Basic assumptions

In this study, the following assumptions were adopted:

1) Soil grains are incompressible.
2) Thermal variation is zero.
3) Pore water density is constant.
4) Pore water acceleration relative to the soil skeleton is negligible.
5) Pore air pressure is zero and constant.
6) Pore air density is negligible compared with pore water and soil grain densities.
7) Effective stress of unsaturated soils is defined based on Bishop[2].

2.2 Governing equations

The multi-dimensional consolidation theory proposed by Biot[3] was used to obtain the governing equations. The governing equations used in this study are stated below.

The momentum balance equation for the soil–water mixture is given by Eq. (1).

$$\rho\mathbf{a} = \nabla\cdot\boldsymbol{\sigma} + \rho\mathbf{b} \tag{1}$$

where ρ is the density of the soil–water mixture, which is expressed as $\rho = (1-n)\rho_\mathrm{s} + n\rho_\mathrm{w}$, n is the porosity of the soil skeleton, ρ_s is the density of the soil grains, ρ_w is the water density, $\mathbf{a}$ is the acceleration of the soil skeleton, $\boldsymbol{\sigma}$ is the total stress of the soil–water mixture, and $\mathbf{b}$ is the gravity vector. The effective stress principle is given by Eq. (2) based on Bishop's effective stress definition[2].

$$\boldsymbol{\sigma}' = (\boldsymbol{\sigma} - P_\mathrm{a}\mathbf{I}) + \chi(P_\mathrm{a} - P_\mathrm{w})\mathbf{I} \tag{2}$$

where $\boldsymbol{\sigma}'$ is the effective stress, P_a is the pore air pressure, P_w is the pore water pressure, χ is the parameter related to the degree of saturation, and $\mathbf{I}$ is Kronecker delta. The suction is expressed as $\mathrm{s} = P_\mathrm{a} - P_\mathrm{w}$. In this study, the value $-P_\mathrm{w}$ is equal to the suction because the pore air pressure is assumed to be zero. Moreover, assuming χ is equal to S_r (S_r is the degree of saturation), the effective stress principle can be expressed as Eq. (3).

$$\boldsymbol{\sigma}' = \boldsymbol{\sigma} + S_r s\mathbf{I} \tag{3}$$

The generalized Darcy's equation is written as Eq. (4).

$$\mathbf{w} = -\frac{kk_{rw}}{\gamma_\mathrm{w}}(\nabla P_\mathrm{w} + \rho_\mathrm{w}\mathbf{a} - \rho_\mathrm{w}\mathbf{b}) \tag{4}$$

where $\mathbf{w}$ is Darcy's velocity, k is the hydraulic conductivity, k_{rw} is the relative permeability, kk_{rw} represents the coefficient of the unsaturated permeability, and γ_w is the unit weight of the pore water.

The mass balance equation for the pore water can be written as Eq. (5).

$$\nabla\cdot\mathbf{w} + S_r\nabla\cdot\mathbf{v} + S_r\frac{n}{K_\mathrm{w}}\dot{P}_\mathrm{w} + n\dot{S}_r = 0 \tag{5}$$

where K_w is the bulk modulus of the pore water, $\mathbf{v}$ is the velocity of the soil skeleton, and ($\dot{\cdot}$) above the variables represent the derivative with respect to time. The fourth term on the left side of Eq. (5) is expressed as

$$n\dot{S}_r = n\frac{\mathrm{d}S_r}{\mathrm{d}t} = n\frac{\mathrm{d}S_r(P_W)}{\mathrm{d}P_W}\frac{\mathrm{d}P_W}{\mathrm{d}t} = C_s\dot{P}_\mathrm{w} \tag{6}$$

where C_s is the specific moisture capacity. By substituting Eq. (6) in Eq. (5), Eq. (7) is obtained.

$$\dot{P}_\mathrm{w} = -\left(\frac{nS_r}{K_\mathrm{w}} + C_s\right)^{-1}(\nabla\cdot\mathbf{w} + S_r\nabla\cdot\mathbf{v}) \tag{7}$$

2.3 Unsaturated seepage characteristics

Unsaturated seepage characteristics are defined based on the relationship between the degree of saturation and suction. This relationship is called the soil–water retention curve. In this study, the van Genuchten retention curve[4], which is one of the representative models, was used. The equation of this model is given in Eq. (8).

$$S_\mathrm{r} = \left[1 + \left(\alpha'\frac{s}{\gamma_w}\right)^{n'}\right]^{-\mathrm{m}'} \tag{8}$$

where α', n', m' are the parameters that determine the shape of the curve, and m' is given by $\mathrm{m}' = 1 - 1/n'$.

By differentiating Eq. (8) with the pore water and substituting it in Eq. (6), the equation for the specific moisture capacity is obtained. This is given in Eq. (9).

$$C_s = \frac{n}{\gamma_w}\alpha'(n'-1)S_\mathrm{r}^{\frac{1}{\mathrm{m}'}}\left(1 - S_\mathrm{r}^{\frac{1}{\mathrm{m}'}}\right)^{\mathrm{m}'} \tag{9}$$

Furthermore, the relative permeability is correlated with the degree of saturation. In this study, the Hillel expression[5] that is given in Eq. (10) was adopted to obtain the relative permeability.

$$k_{rw} = (S_\mathrm{r})^L \tag{10}$$

where L is the fitting parameter and typically has a value ranging from 2 to 4. A value of 2 was used in this study.

2.4 Constitutive model for unsaturated soils

The simple constitutive model for unsaturated soils was proposed by Yerro[6]. This model was formulated based on the Mohr-Coulomb model and adopted Bishop's effective stress (Eq. (2)) as the definition of the stress components in Mohr-Coulomb yield criteria. Additionally, the suction dependence was accounted for in the definition of the cohesion and the friction angle, which are the soil shear strength parameters.

In this study, by referring to the constitutive model by Yerro[6], the Drucker-Prager model extended to unsaturated soils was used, and the non-associated flow rule was adopted in this model. The yield function and plastic potential function are given by Eq. (11) and Eq. (12), respectively.

$$f = \sqrt{J_2} + \eta\bar{I}_1 - \xi c \tag{11}$$

$$g = \sqrt{J_2} + 3\bar{I}_1\sin\psi \tag{12}$$

where f is the yield function, g is the plastic potential function, J_2 is the second invariant of the deviatoric stress tensor, $\bar{I}_1$ is the first invariant of Bishop's effective stress

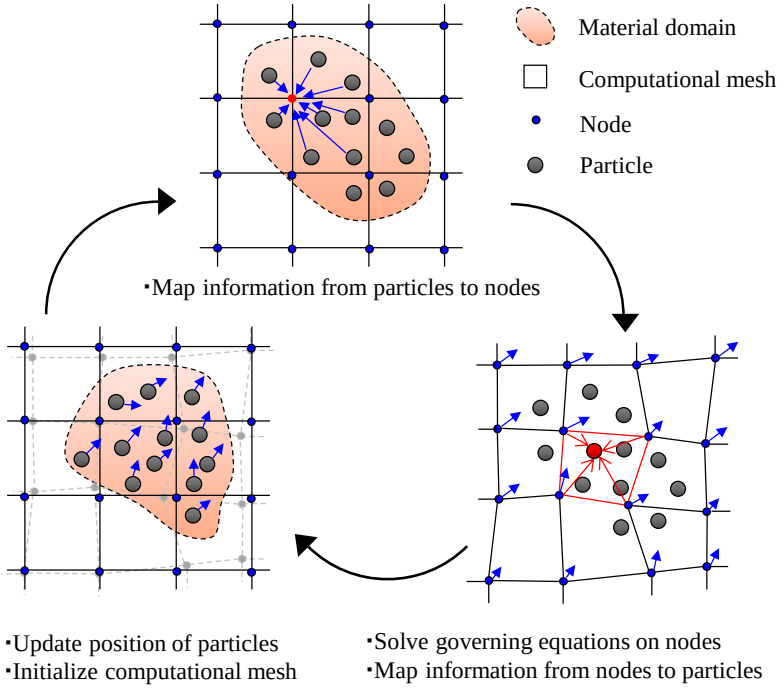

Fig. 1　MPM Algorithm

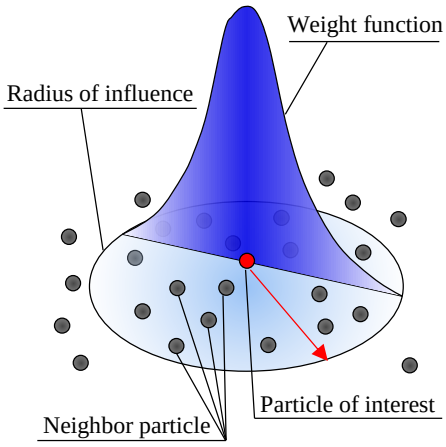

Fig. 2　SPH Approximation

tensor[2], c is the cohesion, ψ is the dilatancy angle, and η and ξ are the coefficients related to the friction angle. Since the problems discussed in this paper are the two-dimensional condition (plane strain condition), η and ξ are given as Eq. (13) and Eq. (14), respectively.

$$\eta = \frac{\tan\phi}{\sqrt{9 + 12\tan^2\phi}} \tag{13}$$

$$\xi = \frac{3}{\sqrt{9 + 12\tan^2\phi}} \tag{14}$$

where ϕ is the friction angle.

Considering the suction dependence, the cohesion and friction angle are defined as Eq. (15) and Eq. (16).

$$c = c' + \Delta c_{max}\left(1 - e^{-B\left(\frac{s}{P_{atm}}\right)}\right) \tag{15}$$

$$\phi = \phi' + A\left(\frac{s}{P_{atm}}\right) \tag{16}$$

where c' is the cohesion in the saturated condition, ϕ' is the friction angle in the saturated condition, Δc_{max} is the maximum increment of the cohesion, P_{atm} is the atmospheric pressure ($= 101.325$kPa), B is the parameter for the cohesion and suction, and A is the parameter for the friction angle and suction.

2.5　Numerical implementation

This section describes the new meshless method that combines the material point method (MPM) and smoothed particle hydrodynamics (SPH), which are two of the representative meshless methods. The momentum balance equation (Eq. (1)) is discretized using MPM, and the generalized Darcy's law (Eq. (4)) and the mass balance equation for the pore water (Eq. (5)) are discretized using SPH.

In both MPM and SPH, the continuum body is represented by a set of particles that carry physical properties of the continuum, such as velocities, stresses, strains, and other state parameters. By using the same particles in both MPM and SPH, the coupled algorithm can be implemented.

Fig. 1 illustrates the MPM algorithm for a single calculation of a time increment. In the MPM algorithm, the computational mesh is used for the calculation together with the particles. At the beginning of each step, the physical properties are mapped from the particles to the nodes of the computational mesh. In the next step, a governing equation is solved for unknown variables on the nodes by using the computational mesh, and the physical properties of the particles are interpolated from the obtained nodal values. The computational mesh does not store any permanent information and is reset at the end of each time step. This means that all variables in the nodes and mesh distortion are discarded at the end of each time step. Finally, the variables and positions of the particles are updated. Fern *et al.*[7] provide a thorough description of the MPM algorithm.

In the MPM algorithm, the boundary conditions should be applied to the nodes because the governing equations are solved on the nodes similar to that in the finite element method (FEM). However, it is expected that the particles near the ground surface will be largely displaced during a slope failure. If the flux boundary conditions for the infiltration of rainfall are applied on the nodes, the nodes given in the boundary conditions have to be redefined along with the motion of the particles because the computational mesh is unable to capture the deformation of the ground surface. Therefore, it is convenient that the flux boundary conditions are directly

applied to the particles because the boundary conditions are automatically moved along with the particle motion.

Hence, in the proposed method, the governing equations related to the pore water are solved by using the SPH algorithm, in which only particles are used for the calculation. Fig. 2 shows the schematic of the SPH approximation. The physical properties can be calculated by interpolating from the neighboring particles inside the domain, called the influence radius. A detailed description of the SPH algorithm can be found in Bui *et al.*[8)]

Based on the MPM framework, the momentum balance equation for the soil–water mixture given in Eq. (1) can be discretized as Eq. (17).

$$M_i \mathbf{a}_i = -\sum_{\mathrm{p}=1}^{N_\mathrm{p}} \mathbf{G}_{i\mathrm{p}} \cdot \boldsymbol{\sigma}_\mathrm{p} V_\mathrm{p} + \sum_{\mathrm{p}=1}^{N_\mathrm{p}} \boldsymbol{\tau}_\mathrm{p} h^{-1} N_i(\mathbf{x}_\mathrm{p}) V_\mathrm{p} + \sum_{\mathrm{p}=1}^{N_\mathrm{p}} m_\mathrm{p} \mathbf{b}_\mathrm{p} N_i(\mathbf{x}_\mathrm{p}) \tag{17}$$

where subscript i represents the variables related to the nodes and subscript p represents the variables related to the particles. M is the lamped mass matrices, V is the volume of the particle, $\boldsymbol{\tau}$ is the prescribed traction, h^{-1} is the boundary layer thickness that is assigned to be equal to the diameter of the particles, m is the mass of a particle, N is the shape function, $\mathbf{G}$ is the gradient of the shape function, and N_p is the number of particles per element.

The generalized Darcy's law given in Eq. (4) can be discretized by using SPH, as shown in Eq. (18).

$$\mathbf{w}_\mathrm{p} = -\frac{k_\mathrm{p} k_{rw,\mathrm{P}}}{\gamma_\mathrm{w}} \sum_{\mathrm{p}'=1}^{N_{\mathrm{p}'}} (P_{\mathrm{wp}'} - P_{\mathrm{wp}}) \boldsymbol{\nabla} \phi_{\mathrm{pp}'} - \frac{k_\mathrm{p} k_{rw,\mathrm{P}}}{g} \left(\sum_{\mathrm{p}'=1}^{N_{\mathrm{p}'}} \mathbf{a}_{\mathrm{p}'} \phi_{\mathrm{pp}'} - \sum_{\mathrm{p}'=1}^{N_{\mathrm{p}'}} \mathbf{b}_{\mathrm{p}'} \phi_{\mathrm{pp}'} \right) \tag{18}$$

where subscript p' indicates the neighboring particles of p, $N_{\mathrm{p}'}$ is the number of p', ϕ is the interpolation function, and $\boldsymbol{\nabla}\phi$ is the gradient of the interpolation function.

As with the discretization of the generalized Darcy's law, the mass balance equation of pore water can be discretized by using SPH, as shown in Eq. (19).

$$\Delta P_{\mathrm{wp}} = -\Delta t \left(\frac{n_\mathrm{p} S_{r,\mathrm{p}}}{K_{\mathrm{w,p}}} + C_{s,\mathrm{p}} \right)^{-1} \sum_{\mathrm{p}=1}^{N_{\mathrm{p}'}} (\mathbf{w}_{\mathrm{p}'} - \mathbf{w}_\mathrm{p}) \boldsymbol{\nabla} \phi_{\mathrm{pp}'} - \Delta t \left(\frac{n_\mathrm{p} S_{r,\mathrm{p}}}{K_{\mathrm{w,p}}} + C_{s,\mathrm{p}} \right)^{-1} \sum_{\mathrm{p}=1}^{N_{\mathrm{p}'}} (S_{r,\mathrm{p}'} \mathbf{v}_{\mathrm{p}'} - S_{r,\mathrm{p}} \mathbf{v}_\mathrm{p}) \boldsymbol{\nabla} \phi_{\mathrm{pp}'} \tag{19}$$

where Δt is the time increment of each step. The pore water pressure increment is calculated using Eq. (19), implying that Eq. (19) is the constitutive equation for the pore water.

2.6 Computational cycle

The computational scheme of the proposed method can be described as follows:

1) Nodal acceleration of the soil skeleton is calculated by solving the momentum balance equation for the soil–water mixture (Eq. (17)).
2) Velocities and strain rate of each particle are calculated by interpolating from nodal acceleration.
3) Effective stress increment of each particle is calculated using the constitutive equations (Eq. (11)–Eq. (16)).
4) Displacement and position of each particle are updated according to particle velocities.
5) All information about the nodes is discarded, and the distortion of the computational mesh is reset to zero.
6) Darcy's velocities of each particle are calculated by solving the generalized Darcy's law (Eq. (18)).
7) Pore water pressure increment of each particle is calculated from the mass balance equation for pore water, and pore water pressure and suction are updated.
8) Degree of saturation, specific moisture capacity and relative permeability of each particle are updated by using Eq. (8)–Eq. (10).
9) Total stress of each particle is updated based on the effective stress principle (Eq. (3)).

3. Validation of the proposed method

It is difficult to directly validate the proposed method because an analytical solution to the problems of unsaturated soils is unavailable. This study selected the drainage of a sand column experiment conducted by Liakopoulos[9)] to validate the proposed method. This experiment was used to validate several numerical codes (e.g., Bandara *et. al.*[10)]) in the past.

Fig. 3(a) shows the schematic of the experiment. Water was allowed to flow at a constant speed from the top to the bottom of the sand column with a height of 1.0 m, and the suction in the sand column was measured starting from the time when the supply of water from the top was stopped. The sand column comprised of Del Monte sand, and the following equations were obtained from the experiment as its hydraulic properties:

$$S_r = 1 - 0.10152 \left(\frac{s}{\gamma_w} \right)^{2.4279} \tag{20}$$

$$k_\mathrm{rw} = 1 - 2.207(1 - S_r) \tag{21}$$

Fig. 3(b) shows the schematic of the numerical model. The length of the computational mesh was 0.04m, and four particles were arranged inside one mesh. The displacement of the bottom of the sand column was fixed, and the displacement of both sides were constrained only horizontally. The impermeable conditions were imposed on the top and the both sides, and the zero water pressure condition was applied to the bottom. Eq. (20) and Eq. (21) were used as the unsaturated seepage characteristics in this calculation. The soil column was modeled as a linear elastic material. Table 1 lists the material parameters, which were determined by referring to the previous

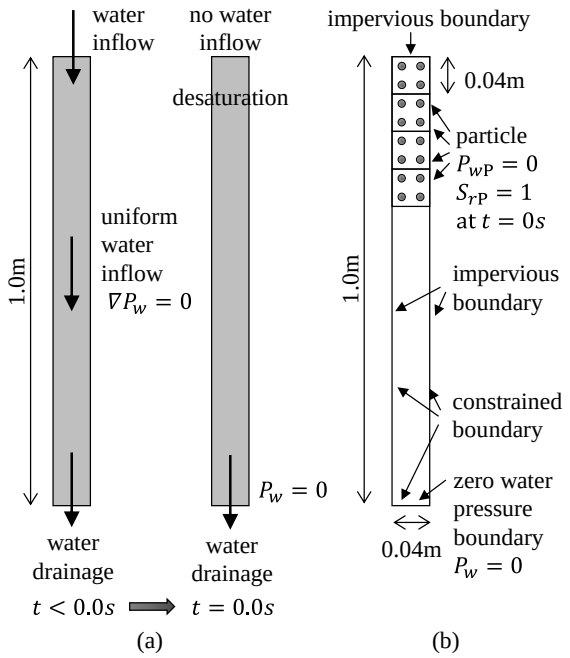

Fig. 3　Liakopoulos Test and Numerical Analysis Model

Table 1　Material Parameters for Liakopoulos

Parameters	Symbol	Value	Unit
Young's modulus	E	1.3	MN/m^2
Poisson ratio	ν	0.4	-
Initial porosity	n	0.2975	-
Soil grain density	ρ_s	2000	kg/m^3
Water density	ρ_w	1000	kg/m^3
Water bulk modulus	K_w	2.0×10^3	MN/m^2
Hydraulic conductivity	k	4.41×10^{-6}	m/s

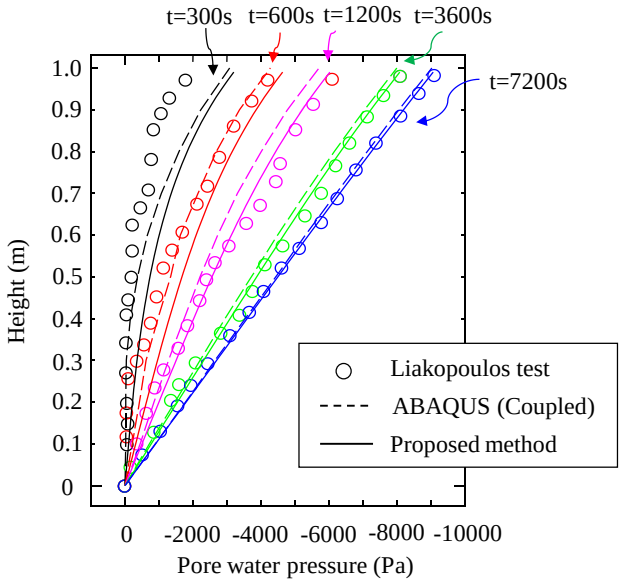

Fig. 4　提案手法と実験値およびABAQUSによる計算値の比較
Comparison of Proposed Method with Experiments and ABAQUS

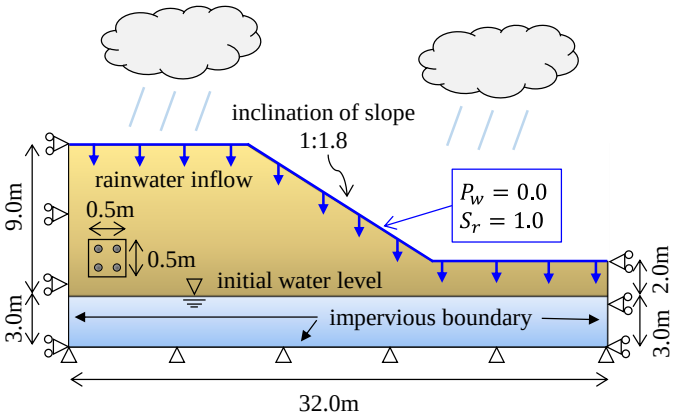

Fig. 5　Slope Geometry for Numerical Analysis

Table 2　Material Parameters for Numerical Analysis

Parameters	Symbol	Value	Unit
Young's modulus	E	10.0	MN/m^2
Poisson ratio	ν	0.33	-
Initial porosity	n	0.35	-
Soil grain density	ρ_s	2700	kg/m^3
Water density	ρ_w	1000	kg/m^3
Water bulk modulus	K_w	2.0×10^3	MN/m^2
Cohesion	c'	1.0	kPa
Effective friction angle	ϕ'	25.0	°
Maximum cohesion	Δc_{max}	100.0	kPa
D-P model parameter	A	0.0	-
D-P model parameter	B	0.07	-
Hydraulic conductivity	k	1.0×10^{-5}	m/s
van Genuchten parameter	α'	0.05	m^{-1}
van Genuchten parameter	n'	3.0	-

study (Bandara *et al.*[10]).

Fig. 4 presents the results from the proposed method as well as the experimental results and the results from ABAQUS[11], which is a software used for FEM. Despite a minimal gap between the results from the proposed method and the experimental results at t = 300 s, the results agreed with the experimental results after t = 600 s. Furthermore, the results from the proposed method were almost identical to the results from ABAQUS[11]. These results confirmed the validity and accuracy of the proposed method

4.　Numerical analysis of slope failure

4.1　Numerical model and material properties

Fig. 5 shows the geometry of the slope. To simplify the problem, the homogeneous embankment was adopted as the slope. The slope had a height of 7.0 m and an inclination of 1:1.8. The initial groundwater level was set at 3.0 m from the bottom of the model. The fixed displacement boundary

condition and the impermeable boundary condition were applied to the bottom of the model. The horizontal displacement was fixed on and the undrained condition was applied to both sides. The square mesh with a length of 0.5 m was adopted as the computational mesh, and four particles were arranged inside one mesh.

Table 2 lists the material properties, which were determined by referring to the slope failure analysis of the sandy clay ground conducted by Yerro[6]. The Drucker-Prager model, proposed in 2.4, was used as the constitutive model.

The initial stress condition was determined by carrying out a self-weight analysis that included only the gravitational acceleration. The initial suction and pore water pressure were determined from the result of the unsaturated seepage analysis. For simplicity, the infiltration of rainfall was modeled by applying the zero water pressure condition to the surface of the ground. Numerical analyses were conducted until a slope failure occurred or an equilibrium condition was reached.

Fig. 6 illustrates the soil–water retention curve used in the numerical analysis, which is given by Eq. (8). The shape of the curve was determined by the water retention curve parameters, α' and n'. The values of these parameters were determined based on the realistic behavior of soil, as listed in Table 2. In the initial stress condition, the degree of saturation of each part of the slope ranged from 95% to 100%, depending on the suction which was determined using the results of the unsaturated seepage analysis. The possible range of the soil–water retention curve in the analysis is indicated by the solid line in Fig. 6.

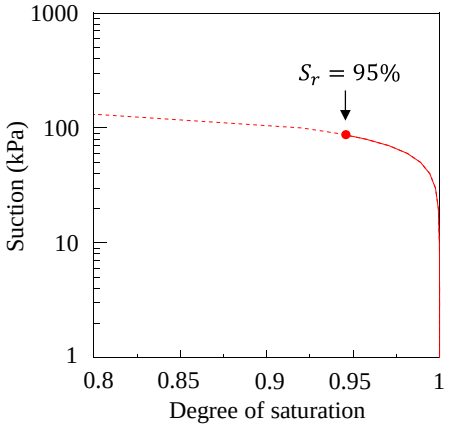

Fig. 6 Soil-Water Retention Curve

In the following sections, the rainfall-induced slope failure process is presented, first, based on the results of the numerical analysis. Then, to investigate the influence of the rainwater infiltration characteristics of unsaturated soils on a magnitude of slope failure, as well as the time required for a slope failure to occur, the parametric studies about the degree of saturation, water retention, and permeability are discussed.

4.2 Slope failure process

Fig. 7 shows the suction contours at three different times and the position of the water level. Fig. 7(a) shows the suction distribution immediately after the start of infiltration. In this stage, the water level does not change from its original position, which is shown in Fig. 5. Fig. 7(b) and Fig. 7(c) show that the water level near the surface of the slope rises as the time progresses. In addition, the value of the suction inside the slope gradually decreases due to the rainfall infiltration.

Fig. 8 illustrates the deviatoric strain contours at three different times and the position of the water level. In Fig. 8(b), a slope failure occurs in the saturated part under the water level, which implies that the slope failure was caused by a decrease in the soil strength due to a decrease in the suction. As the slope continues to be saturated, the position of the water level near the slope surface becomes higher, and the slope failure zone becomes deeper and progresses toward the upper part of the

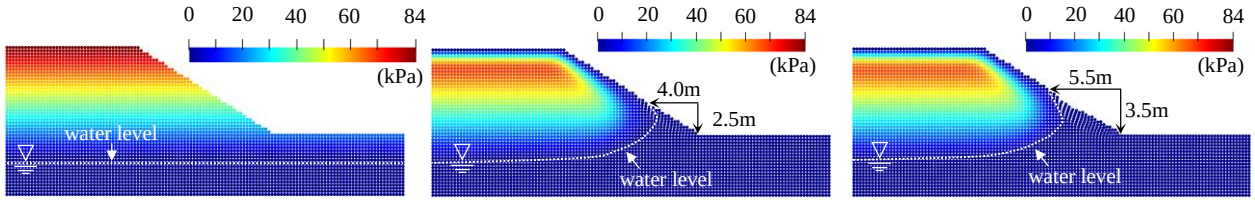

(a) $t = 0s$　(b) $t = 100s$　(c) $t = 150s$

Fig. 7　Suction Contours at Different Times

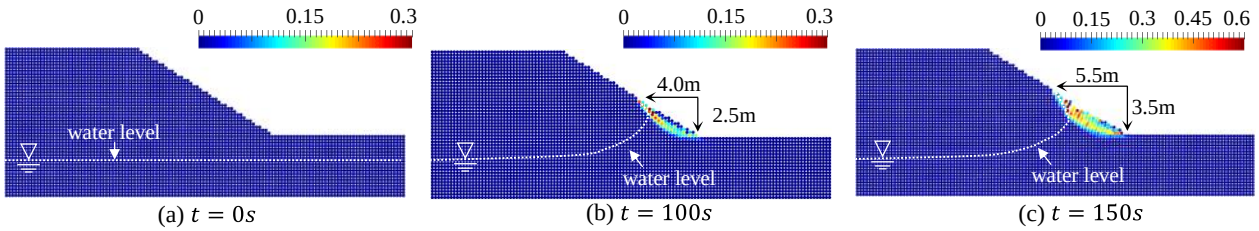

(a) $t = 0s$　(b) $t = 100s$　(c) $t = 150s$

Fig. 8　Deviatoric Strain Contours at Different Times

slope. During the analysis, the failure zone was observed only in the saturated zone and never in the unsaturated zone. Therefore, it can be inferred that the main cause of the slope failure in this analysis was the progressive loss of soil strength.

4.3 Influence of degree of saturation and water retention

To investigate the influences of the degree of saturation and the water retention on the slope failures, a parametric study focusing on both the degree of saturation and the soil–water retention curve was conducted.

The adopted values of the van Genuchten parameters, which determine the shape of the curve (see Eq. (8)), are listed in Table 3, with all other material properties kept the same as in Table 2. These parameters were determined based on the possible values for real soils. The same initial stress and suction conditions, as in 4.1, were used for all three cases, which implies that the initial distributions of the degree of saturation were different for each case.

Fig. 9 illustrates the soil–water retention curves for each case. The possible ranges of the soil–water retention curves are indicated by the solid lines in Fig. 9. The initial degree of saturation at the top of the slope, which is the minimum value in the slope, was 85% in Case W1, 95% in Case W2, and 99.5% in Case W3.

Fig. 10 illustrates the deviatoric strain contours after the slope failures and the vertical and horizontal lengths of the parts of the slope failures. The slope failure in Case W1 was the largest, followed by those in Case W2 and Case W3. In Case W1, which is the almost saturated condition, the failure zone developed in more than half of the slope surface. Thus, it can be deduced that the scales of the slope failures become larger as the degree of saturation becomes higher.

Fig. 11 illustrates the suction contours at the start of the slope failures and the water level. In Case W1, the slope failures occurred when approximately 60 kPa of the suction remained inside the embankment and the water level near the slope surface was the highest among the three cases. On the other hand, in Case W2 and Case W3, the suction inside the embankment was larger than that in Case W1 and the water level was lower when the slope failures occurred. There were minimal differences in the contours between Case W2 and Case W3 (Fig. 11(b) and Fig. 11 (c)). However, the water level near the slope surface in Case W2 was higher than in Case W3. From this, it can be inferred that the scales of the slope failures become lager as the water level near the slope surface becomes

Table 3 van Genuchten Parameters for Parametric Study

	CaseW1	CaseW2	CaseW3
van Genuchten parameter α'	0.025	0.05	0.074
van Genuchten parameter n'	3.0	3.0	3.0
Degree of saturation	99.5-100 %	95-100 %	85-100 %

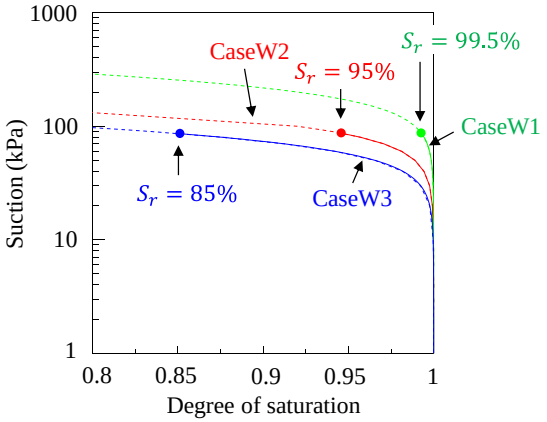

Fig. 9 Soil-Water Retention Curve for Each Case

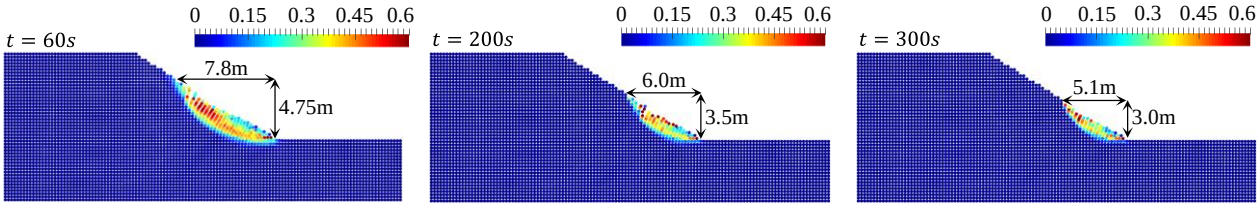

(a) Case W1 (S_r=99.5-100%)　(b) Case W2 (S_r=95-100%)　(c) Case W3 (S_r=85-100%)

Fig. 10 Deviatoric Strain Contours after Slope Failures in Cases of Retention Curve Parametric Study

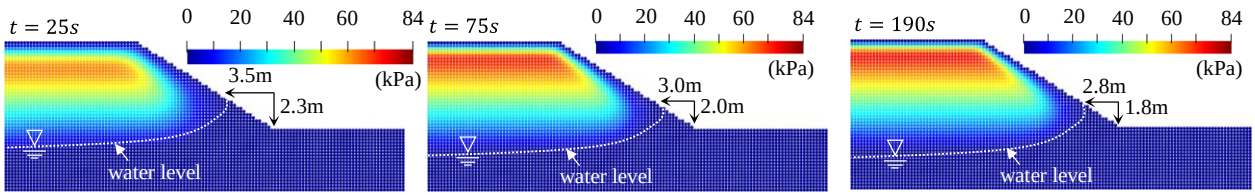

(a) Case W1 (S_r=99.5-100%)　(b) Case W2(S_r=95-100%)　(c) Case W3 (S_r=85-100%)

Fig. 11 Suction Contours at Start of Failures in Cases of Retention Curve Parametric Study

higher when slope failures occur.

Fig. 12 shows the verification points of the displacement and suction inside the embankment. Considering the position of the slope failures, the verification points were located at the lower half of the slope.

Fig. 13 shows the evolution of the displacement at the measurement points (A1, A2, B1, B2, C1, and C2) and the start time of the slope failure. The start times of the slope failure for each case became earlier as the degree of saturation became higher. In Case W1, the displacement at C1 was the largest among all the verification points. On the other hand, in Case W2 and Case W3, the displacement at B1 was the largest and the displacement at C1 was almost zero during the analysis. This is because the slope failure reached more than half of the slope only in Case W1, as shown in Fig. 11.

Fig. 14 shows the evolution of the suction at the verification points (B1, B2, and B3) and the start time of the slope failure. The dissipation speed of suction became faster as the degree of saturation became higher. The slope failures occurred when the suction at all three verification points (B1, B2, and B3) was reduced to negative values. Hence, it can be inferred that the lower part of the slope was weak enough to induce the slope failures at these points as the lower part of the slope became saturated.

From these results, it can be understood that the scale of the slope failure and the time to reach the slope failure depend on the water retention and the degree of saturation.

It should be noted that the failure processes for all cases were the same as in 4.2, implying that the failures were induced not by the loss of lateral support, but the loss of the soil strength. Because of length constraints, the details of the failure processes for the three cases are omitted in this paper.

4.4　Influence of permeability

A parametric study focusing on the hydraulic conductivity was conducted to examine the influence of soil permeability on slope failures. The adopted values of hydraulic conductivity are listed in Table 4, with all other material properties kept the same as in Table 2. The same initial stress and suction conditions, as in 4.1, were used for all three cases. The same values of the van Genuchten parameters, as in Case W1 in 4.3, were used in all three cases. Hence, the range of the degree of saturation was also equal to that in Case W1.

Fig. 15 shows the deviatoric strain contours after the slope failures and the vertical and horizontal lengths of the parts of the slope failures. The scales of the slope failures became larger as the hydraulic conductivity increased. From this result, it can

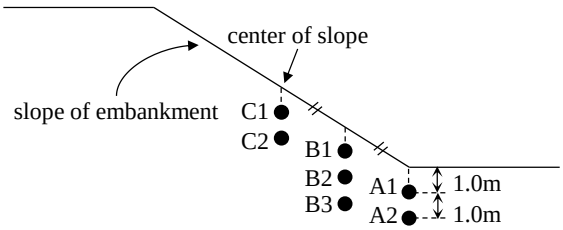

Fig. 12　Verification Points of Displacement and Suction

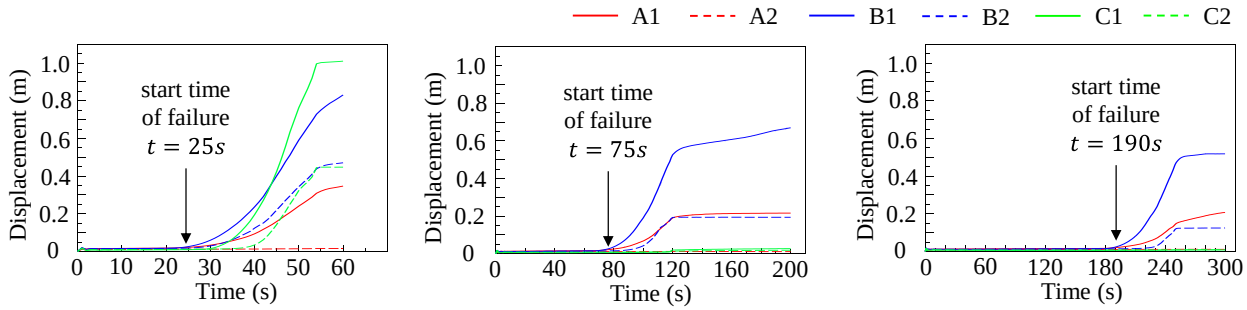

(a) Case W1 (S_r=99.5-100%)　(b) Case W2 (S_r=95-100%)　(c) Case W3 (S_r=85-100%)

Fig.13　Evolution of Displacement at Verification Points in Cases of Retention Curve Parametric Study

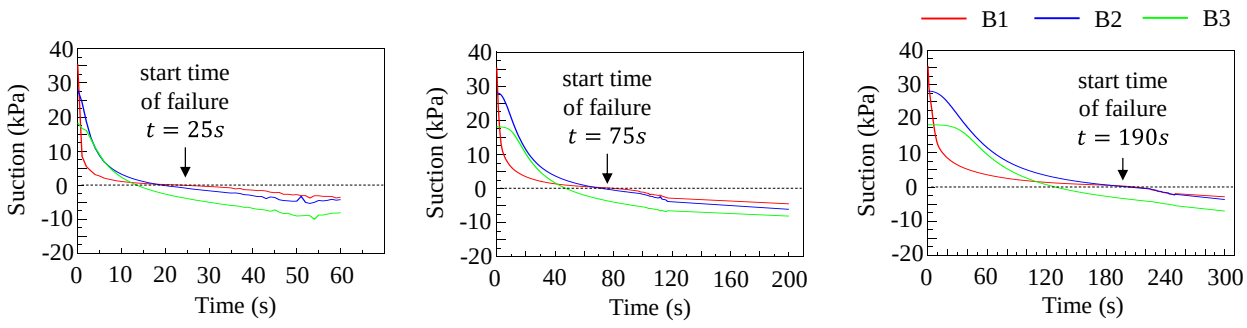

(a) Case W1 (S_r=99.5-100%)　(b) Case W2 (S_r=95-100%)　(c) Case W3 (S_r=85-100%)

Fig. 14　Evolution of Suction at Verification Points: B1~B3 in Cases of Retention Curve Parametric Study

be inferred that the hydraulic permeability can influence the scale of the slope failure.

The suction contours at the start time of the slope failures and the position of the water levels are illustrated in Fig. 16. It can be observed that the position of the water level near the slope became higher as the hydraulic conductivity increased. This can be attributed to the fact that the rainfall infiltration speed in the slope surface increases as the hydraulic conductivity becomes higher.

Fig. 17 shows the evolution of the displacement at the

Table 4　Hydraulic Conductivity for Parametric Study

	Case H1	Case H2	Case H3
Hydraulic conductivity k	1.0×10^{-4} m/s	1.0×10^{-5} m/s	1.0×10^{-6} m/s
van Genuchten parameter α'	0.05		
van Genuchten parameter n'	3.0		
Degree of saturation	95-100 %		

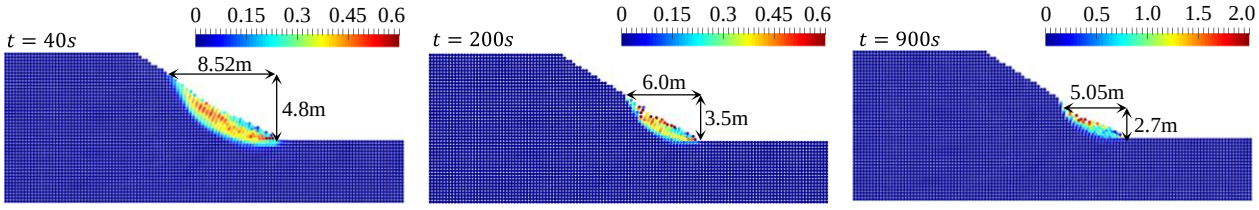

(a) Case H1 ($k = 1.0\times10^{-4}$ m/s)　(b) Case H2 ($k = 1.0\times10^{-5}$ m/s)　(c) Case H3 ($k = 1.0\times10^{-6}$ m/s)

Fig.15　Deviatoric Strain Contours after Slope Failures in Cases of Hydraulic Conductivity Parametric Study

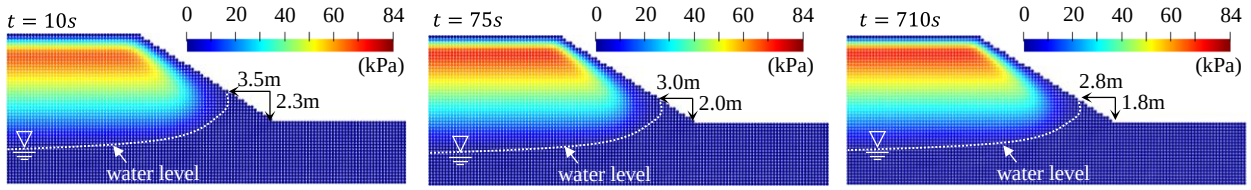

(a) Case H1 ($k = 1.0\times10^{-4}$ m/s)　(b) Case H2 ($k = 1.0\times10^{-5}$ m/s)　(c) Case H3 ($k = 1.0\times10^{-6}$ m/s)

Fig.16　Suction Contours at Start of Failures in Cases of Hydraulic Conductivity Parametric Study

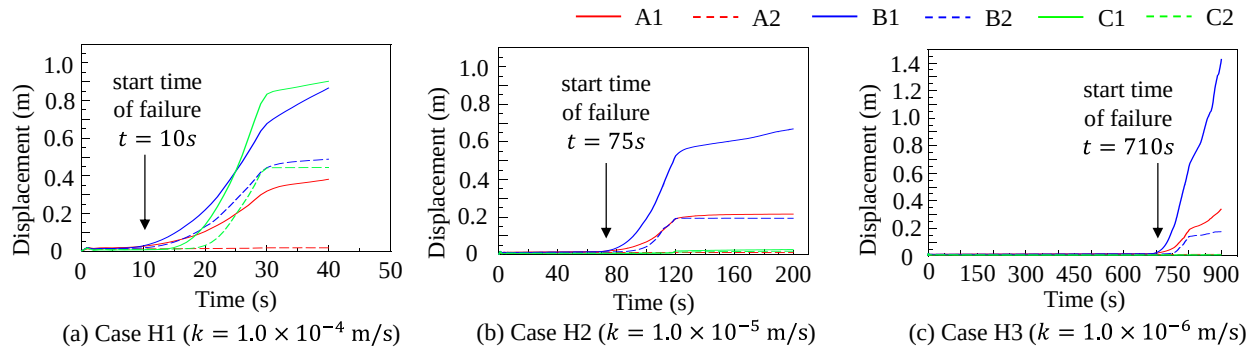

(a) Case H1 ($k = 1.0\times10^{-4}$ m/s)　(b) Case H2 ($k = 1.0\times10^{-5}$ m/s)　(c) Case H3 ($k = 1.0\times10^{-6}$ m/s)

Fig. 17　Evolution of Displacement at Verification Points in Cases of Hydraulic Conductivity Parametric Study

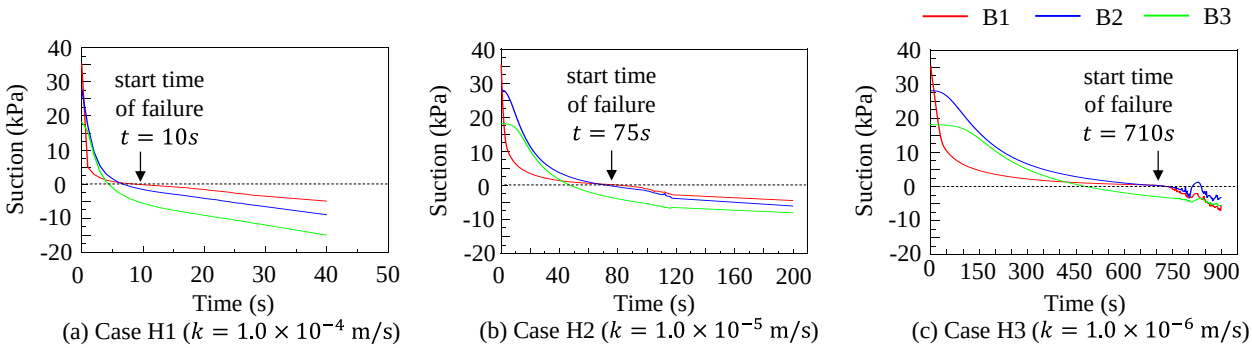

(a) Case H1 ($k = 1.0\times10^{-4}$ m/s)　(b) Case H2 ($k = 1.0\times10^{-5}$ m/s)　(c) Case H3 ($k = 1.0\times10^{-6}$ m/s)

Fig. 18　Evolution of Suction at Verification Points: B1~B3 in Cases of Hydraulic Conductivity Parametric study

verification points (A1, A2, B1, B2, C1, and C2) and the start time of the slope failure. The start time of the slope failure became earlier as the hydraulic conductivity became higher. The displacement of C1 was remarkable in Case H1 because the slope failure zone reached near the top of the slope only in Case H1, as shown in Fig. 15 (a). The displacement of B1 in Case H3 was much larger than those in the other two cases, although the collapse scale was the smallest. This is because the local deformation near B1 was remarkable in Case H3.

Fig. 18 shows the evolution of the suction at the verification points (B1, B2, and B3) and the slope failure start time. The dissipation speed of suction became faster as the hydraulic conductivity became larger. As with the previous parametric study in 4.3, the slope failures occurred when the suction at the three verification points (B1, B2, and B3) became negative. Hence, it can be confirmed that the loss of suction in the lower part of the slope was an important factor causing a slope failure.

From these results, it can be inferred that hydraulic conductivity can influence the scale of and time required for the slope failure.

5. Summary

In this study, the new meshless method using MPM and SPH was proposed for simulating the slope failures induced by rainfall. The conclusions of this paper are as follows:

1) The new meshless method coupled MPM and SPH was proposed for simulating slope failures.
2) Simulation of the experiment on the unsaturated soil was conducted to verify the accuracy and validity of the proposed method.
3) Numerical analyses of the slope failures were conducted, and the effects of soil saturation, water retention, and permeability on the scale of the slope failures and the time required for slope failures to occur were investigated.
4) The results show that the scale of slope failure, shape of collapse, and time until the slope failure are governed by soil saturation, water retention, and permeability.

In this study, the effect of rainfall was modeled by applying the zero water pressure boundary condition. In the proposed method, the infiltration of rainfall can be considered by directly applying the flux boundary condition to the particles. In future work, the rainfall intensity will be investigated.

References

1) Ministry of Land, Infrastructure and Transport: Occurrence of sediment-related disasters in 2019, 2020
2) Bishop, A. W.: The principal of effective stress, Norwegian Geotechnical Institute, 32, pp. 1–5, 1960
3) Biot, M.A.: General theory of three-dimensional consolidation, Journal of Applied Physics, 12(2), pp. 155–164, 1963
4) Genuchten, V. M.: A closed-form equation for predicting the hydraulic conductivity of unsaturated soil. Soil Sci. Soc. Am. J. 44, No.4, pp. 892–898, 1980
5) Hillel, D.: Soil and water – physical principles and processes, London, UK: Academic Press, Inc., 1971
6) Yerro, A.: MPM modelling of landslides in brittle and unsaturated soils, Universitat Politecnica de Catalunya, Ph.D. thesis, 2015
7) Fern, E.J., Rohe, A., Soga, K. and Alonso, E.E.: The Material Point Method for Geotechnical Engineering A Practical Guide, CRC Press, 2019
8) Bui, H.H., Fukagawa, R., Sako, K. and Ohno, S.: Lagrangian meshfree particles method (SPH) for large deformation and failure flows of geotechnical using elastic-plastic soil constitutive model, International Journal for Numerical and Analytical Methods in Geomechanics, 32, pp. 1537–1570, 2008
9) Liakopoulos, A.C.: Transient flow through unsaturated porous media, PhD Thesis, University of California Berkley, 1965
10) Bandara, S., Ferrari, A. and Laloui, L.: Modelling landslides in unsaturated slopes subjected to rainfall infiltration using material point method. International Journal for Numerical and Analytical Methods in Geomechanics, Wiley Online Library, 2015
11) Washington University in St. Louis, School of Engineering & Applied Science: ABAQUS Version 6.6 Documentation, ABAQUS Benchmarks Manual, https://classes.engineering.wustl.edu/2009/spring/mase5513/abaqus/docs/v6.6/books/bmk/default.htm?startat=ch01s08ach66.html (accessed 2020-06-04)